J Therm Spray Tech
https://doi.org/10.1007/s11666-026-02240-3

ORIGINAL RESEARCH ARTICLE

Powder Aerosol Deposition and Electrochemical Characterization of 30 µm thick LLZO Solid Electrolyte as a Separator Layer for Solid-State Batteries

Lukas Hennerici[1,2] · Till Fuchs[3] · Sabrina Lang[5] · Daniel Paulus[1,2] · Mario Linz[1,2] · Dominik Kramer[5] · Reiner Mönig[5] · Jürgen Janek[4] · Daniela Schönauer-Kamin[1,2] · Ralf Moos[1,2]

Submitted: 6 March 2026 / in revised form: 15 April 2026 / Accepted: 26 April 2026

Abstract Garnet-type $Li_7La_3Zr_2O_{12}$ (LLZO) is a promising solid electrolyte (SE) for solid-state batteries (SSBs). However, identifying a suitable processing method to allow dense film fabrication without high sintering temperatures remains challenging. Powder aerosol deposition method (PAD, a.k.a. ADM) enables the fabrication of dense LLZO films at room temperature. To date, studies on PAD-LLZO films primarily addressed the electrical properties in terms of conductivity, while their cycling performance remains largely unexplored. In this study, we show that PAD-LLZO films can be used for the reversible transport of lithium with current densities up to 0.41 mA cm^{-2} with no thermal post-treatment of pristine films after deposition, albeit at high overvoltage. A mild annealing at 400 °C is performed to reduce microstrain, which is known to lead to high overvoltage during cycling in the as-deposited state. Higher ionic conductivities are achieved after annealing, while the cycling stability deteriorates. These phenomena are attributed to reduced compressive stress as well as microstrain after annealing of the PAD-LLZO films with a nanocrystalline microstructure. Based on these assumptions, we propose a possible strategy to improve cycling stability by adapting a post-treatment process to reduce the volume fraction of grain boundaries by controlled grain growth.

Keywords battery fabrication · cycling stability · garnet-type oxides · lithium metal electrode · powder aerosol deposition method (PAD) · solid electrolyte (SE) · solid-state batteries (SSBs)

✉ Lukas Hennerici
Lukas.Hennerici@uni-bayreuth.de

✉ Ralf Moos
functional.materials@uni-bayreuth.de

1 Department of Functional Materials, University of Bayreuth, Universitätsstraße 30, 95447 Bayreuth, Germany

2 Bayerisches Zentrum für Batterietechnik, Weiherstraße 26, 95448 Bayreuth, Germany

3 Institute of Experimental Physics I and Center for Materials Research, Justus-Liebig-University Gießen, Heinrich-Buff-Ring 16, 35392 Gießen, Germany

4 Institute of Physical Chemistry and Center for Materials Research, Justus-Liebig-University Gießen, Heinrich-Buff-Ring 17, 35392 Gießen, Germany

5 Institute for Applied Materials, Karlsruhe Institute of Technology, Herrmann-von-Helmholtz-Platz 1, 76344 Eggenstein-Leopoldshafen, Germany

Introduction

Thriving toward large-scale application of solid-state batteries (SSBs) in industry and especially in the transportation sector, various solid electrolytes (SE)—sulfides, thiophosphate, oxides, or polymers—to name a few, have demonstrated encouraging characteristics. In general, the application of a SE separator may enable the utilization of lithium metal anodes by avoiding the use of flammable liquid electrolytes (Ref 1-4). Suitable separator SEs must exhibit properties like high ionic conductivity and stability against dendrite growth essential for increased safety. Furthermore, they must support high current densities for high power densities, as well as large energy densities of SSBs to compete with their conventional liquid-based lithium-ion battery (LIB) counterparts. Finally, an economically viable fabrication process for processing the SE material must be established to enable large-scale use.

The lithium-stuffed garnet-type oxide $L_7La_3Zr_2O_{12}$ (LLZO) with its cubic crystal structure exhibits high mechanical and thermodynamic stability, as well as a wide

Published online: 21 June 2026

electrochemical stability window (voltage range) (Ref 4-6). Several studies have shown that LLZO can reach ionic conductivities up to 10^{-3} S cm^{-1} even at room temperature (Ref 4, 7, 8). Such ionic conductivities of the separator electrolyte exceed the minimum requirement of at least 10^{-4} S cm^{-1} needed when cells with an area loading of 5 mAh cm^{-2} and charging rates with C-rates above 1 C are targeted.

The electrochemical properties, especially the maximum current densities and ionic conductivities, of LLZO are commonly investigated using mm-thick pellets that have to be sintered and densified at temperatures exceeding 1000 °C, which is far from realistic industrial application. Two challenges are evident for commercial application in SSBs: On the one hand, the thickness of the SE separator layer should be drastically reduced to a level suitable for commercial applications to allow for optimized energy densities, while retaining a sufficient ionic conductivity. Therefore, Randau et al. suggested that a film thickness less than 50 µm is required (Ref 9). On the other hand, the sintering step at high temperatures (> 1000 °C) significantly increases the cost of fabrication, especially for large-scale applications. Consequently, from an economic perspective, a process with significantly lower processing temperatures is required—especially for large areas such as those needed for batteries—in order to avoid even higher energy costs in addition to those for the high temperatures already required for powder synthesis.

The use of the powder aerosol deposition method (PAD, also referred to as aerosol deposition method (ADM) or vacuum kinetic spray (VKS)) for the fabrication of LLZO-SE films addresses the aforementioned challenges. PAD enables the fabrication of dense ceramic films (> 95 % of the bulk density) at room temperature, which would significantly reduce the fabrication costs of LLZO films. In addition, thicknesses of a few hundreds of nm to several hundreds of µm can be achieved (Ref 10).

To date, several studies have been published on the fabrication and use of PAD-LLZO films as the SE separator (Ref 11-18). The following summarizes most significant findings: Ahn et al. and Hennerici et al. demonstrated that PAD-LLZO films can be utilized as separator layers for PAD-SSBs, providing a proof of concept (Ref 13, 16). Very recently, Han et al. reported the so far highest ionic conductivity of 10^{-5} S cm^{-1} (determined from the overall resistance of the film) at room temperature in the as-deposited state using an Al-doped LLZO in an in-plane cell setup (Ref 18). The highest conductivity in a through-plane setup with lithium metal as reversible electrode (Cu|LLZO|Li)—meaningful for the application of PAD films in SSBs—was reported by Nazarenus et al. and Hahn et al. (Ref 11, 15). Ionic conductivities of up to 10^{-7} S cm^{-1} at 70 °C were achieved in as-deposited state with an Al/Ta-doped LLZO.

Overall, ionic conductivities reported for PAD-LLZO films in the as-deposited state have not reached the values achieved for bulk LLZO, with a minimum ionic conductivity of 10^{-4} mS cm^{-1} as it is required for a separator layer. Hanft et al. explained this with the influence of the deposition mechanism on the electrochemical properties of PAD-LLZO films (Ref 14). It was shown that the PAD deposition mechanism, in which particles break down into several tens of nanometer-sized particles upon impact with the substrate, leads to a nanocrystalline microstructure as validated by XRD analyses combined with Rietveld refinement. This leads to an increased grain boundary volume fraction in the films, which may be a reason for the reduced effective ionic conductivity in LLZO (Ref 19). In addition, the XRD analyses show that the deposition mechanism induces microstrain, i.e., local variations of the lattice parameters as well as compressive stresses into the film, which is a common feature of PAD films (Ref 14, 20, 21). Especially the microstrain resulting from lattice distortions affects the diffusion channels and leads to reduced ionic conductivity of as-deposited PAD films compared to a typical bulk material (Ref 14).

In literature, different post-treatment methods are suggested to counteract this effect by introducing energy into the film (Ref 12, 14). Doing so, the ionic conductivity for PAD-LLZO films increased up to two orders of magnitude as a result of decreased microstrain. In a half-cell setup (Cu|LLZO|Li) conductivities of up to 10^{-4} S cm^{-1} were achieved after a conventional thermal post-treatment at 400 °C for 1 h (Ref 11, 15).

Nazarenus et al. investigated the cycling behavior in terms of critical current densities (CCD) of PAD-LLZO films in a Cu|LLZO|Li cell setup. A CCD of 300 µA cm^{-2} at an overvoltage of 0.01 V was achieved for a PAD-LLZO film with a thickness of 30 µm annealed at 400 °C for 1 h. However, a voltage drop during earlier stages of the cycling experiment indicates damage of the separator layer already at much lower current densities of only 30 µA cm^{-2} (Ref 11). Such cycling stability remains insufficient for practical applications. Especially, the cycling behavior indicates dendrite growth already at low current densities.

The present study therefore aims to investigate the underlying reasons for the significantly lower cycling stability and CCD of PAD-LLZO films compared to sintered bulk materials. For this purpose, the cycling performance of as-deposited PAD-LLZO films is compared to that of films that were annealed at 400 °C for 1 h, with a particular focus on differences in the film microstructure in terms of grain size and microstrain characterized by XRD. Based on the findings, a potential adaptation of the post-treatment

process—aimed at modifying the film microstructure—is proposed, which may improve the cycling stability of PAD-LLZO films.

Experimental Section

Sample Preparation

Film Fabrication

The cubic phase LLZO powder used for film fabrication was provided by Schott AG, Mainz. It was synthesized with a method based on the procedure described by Hoinkis et al. (Ref 22). The films were fabricated using PAD. Details of the applied PAD process have previously been reported elsewhere (Ref 11, 23). Samples for EIS analysis, Hebb-Wagner polarization, and cycling experiments were deposited on copper metal sheets with a thickness of 500 µm. For XRD analyses, films were fabricated on silicon wafer cuts with (911) orientation (wafer thickness 500 µm).

Thermal Post-treatment of the As-Deposited Films

The samples were annealed in a custom-made tube furnace in inert N_2 atmosphere. Heating and cooling rates were kept at 1 K min^{-1}. Annealing temperature and dwell time were varied between 400 °C and 700 °C as well as 1 h and 48 h for the different samples and will be specified for each individual experiments.

Cell Assembly

Prior to EIS, Hebb-Wagner polarization, and cycling experiments, a lithium metal anode (Ø 3 mm, 0.75 mm thickness) was manually pressed on top of the PAD-LLZO film. A copper substrate was added on top of the lithium metal and served as current collector. Finally, the samples were placed in a PAT-Cell (EL-Cell, Hamburg, Germany). All steps before were conducted in an argon-filled glovebox. A spring force of approximately 50 N (in accordance with data retrieved from the manufacturer, assuming an overall sample thickness of 1.5 mm) was applied. This resulted in an overall pressure of approximately 3 MPa. The PAT-Cell was placed in a PAT-Stand-4 (EL-Cell, Hamburg, Germany), which was located in a climate chamber to maintain a constant temperature during the individual characterization steps.

Characterization Methods

Determination of Film Thickness

Film thicknesses d_{LLZO} for the samples used for electrochemical characterization were determined using a Mahr S2 Perthometer (Carl Mahr Holding GmbH, Göttingen, Germany). For each batch of PAD-LLZO films fabricated, an additional sample was prepared for film thickness measurement, in order to prevent sample contact with surrounding atmosphere prior to other characterization methods. The measured film thickness of samples used in the individual experiments is reported in the supporting information (Table S1).

Determination of the Ionic Conductivity

To determine the activation energy E_A from Arrhenius plots, the temperature was varied in the range from 70 °C to 20 °C. EIS analysis was conducted at different temperatures in potentiostatic mode with an amplitude of 25 mV within the frequency range of 100 kHz to 100 mHz with ten frequency points per decade. The intersection of the real axis of the complex impedance in the Nyquist representation was used to calculate the ionic conductivity σ_{eff} (through-plane).

Determination of the Electronic Conductivity (Hebb-Wagner Polarization)

The electronic conductivity σ_{el} was determined using the Hebb-Wagner polarization method, which polarizes the PAD layer between an ion-blocking electrode (copper) and a reversible electrode (lithium metal). At 70 °C potentials of 0.2, 0.4, and 0.6 V were applied for 15 h each. The electronic current I_{el} was then determined using the current value obtained at the end of the polarization. Before each polarization step and after the last step, EIS analyses were conducted in the galvanostatic mode with an amplitude of 10 µA within the frequency range of 100 kHz to 100 mHz with ten steps per decade. The intersection of the real axis in the Nyquist representation of the complex impedance was used to calculate the ionic conductivity σ_{eff}.

Cycling Experiments

The cycling experiments and EIS analysis during the cycling experiments were performed at 70 °C. Prior to each cycling experiment, a lithium reservoir was electrodeposited into the Cu|LLZO interface to form a symmetrical cell with stacking sequence Cu|Li|LLZO|Li|Cu. To form the lithium reservoir (initial lithium electrodeposition), a current I = 10 µA (ca. 0.05 mA cm^{-2}) was applied for

approximately 3 h, which corresponds to ca. 0.74 µm Li metal.

For the CCD determination, the current density was increased from 20 µA (ca. 0.10 mA cm^{-2}) in steps of 10 µA and afterward in steps of 20 µA until a short circuit occurred. EIS experiments prior to and during cycling experiments were conducted in potentiostatic mode with an amplitude of 25 mV within the frequency range of 100 kHz to 100 mHz with ten steps per decade. Quantitative analyses of the EIS spectra were performed with the software Relaxis 3 (rhd instruments, Darmstadt, Germany).

X-Ray Diffraction

The as-received LLZO powder and the PAD-LLZO films deposited on silicon wafers were analyzed with a D8 Advance X-ray diffractometer XRD (Bruker AXS GmbH, Karlsruhe, Germany) with a copper anode operated at 2.2 kW, a Ge(111) monochromator (λ = 1.5406 Å), and a 1D-Lynxeye-detector in a Bragg-Brentano arrangement. The samples were analyzed in the range between 15° and 60° (2Θ). For the powders, steps of 0.01° for a hold time of 1 s and for the films steps of 0.015° with a hold time of 3 s were used.

Line shapes and positions for the structures were determined using a silicon standard (NIST SRM 640 g). Rietveld refinement to evaluate the received data was performed with the TOPAS-Academic 64 V 7.24 (Coelho Software, Brisbane, Australia) software. Lattice parameters, crystallite size D, and microstrain ε_0 were refined. To model reflex broadening due to size and strain, the double Voigt approach according to Balzar available in the software was employed (Ref 24, 25). Additionally, the texture was modeled using spherical harmonics to minimize the impact of the texture on the intensities of the reflexes (Ref 26). A detailed description of the refinement procedure can be found elsewhere (Ref 27).

Operando Scanning Electron Microscopy

The operando SEM imaging of lithium stripping and plating on a PAD-LLZO film was conducted inside an SEM (Merlin by Carl Zeiss AG, Oberkochen, Germany). The cells were mounted on a 45° SEM holder and transferred from the argon glovebox to the SEM using a transfer system (Leica EM VCT 100). A micromanipulator (Kleindiek Nanomanipulator MM3A) was used to contact the lithium metal electrodes inside the SEM. The copper substrate was connected through the SEM stage to a galvanostat (CompactStat, Ivium Technologies BV, Eindhoven, Netherlands). Backscattered electrons (BSE) with an energy of 18 keV were used for imaging. The large number of BSEs of LLZO led to bright regions in the images. Darker regions in the images correspond to the light elemental lithium metal. The brightness of these regions decreases with the lithium thickness, i.e., with the number of BSEs that are generated in the LLZO and are absorbed on their way through the lithium metal. For stripping and plating, a current of 5 nA (corresponding to roughly 25 nA cm^{-2}) was used. A more detailed description of the experiment can be found elsewhere (Ref 28).

Results and Discussion

Characterization of PAD-LLZO Films in the As-Deposited State

Investigations of PAD-LLZO films are usually performed using electrochemical characterization like cycling experiments and EIS analysis, which indicate that the reversible transport of lithium is possible. Figure 1 displays the visual proof in the form of operando SEM observations of the electrochemical deposition and dissolution of lithium through the PAD layer. A video corresponding to Fig. 1(b and c) can be found in the supporting information (Video S1). In addition to the SEM images, the current-voltage data are shown in Fig. 1(a) where the individual values corresponding to the SEM images from 1 (begin of life (BOL)) to 6 (after plating) are highlighted by blue dots. These results were obtained as part of the study conducted by Lang et al. (Ref 28).

As illustrated in the SEM images and explained in the experimental section, lithium appears dark depending on its thickness, while LLZO appears bright. Upon applying a negative current (stripping, image 1-3, Fig. 1), lithium is dissolved into the electrolyte and forms voids, leading to an increasing exposure of the underlying LLZO film surface. This process can be reversed by applying a positive current (plating image 4-6). Notably, no temperature treatment was applied to the film after powder aerosol deposition. A more detailed evaluation of the operando SEM and an interpretation in terms of the underlying mechanisms of lithium stripping and plating on PAD-LLZO films can be found in the study by Lang et al. (Ref 28). Additional SEM investigations of PAD-LLZO films, including cross-sectional analyses confirming uniformity, continuity, and adhesion, are provided in the studies by Hanft et al. and Nazarenus et al. (Ref 11, 14). Moreover, PAD films are generally believed to reach approximately 95 % of the theoretical material density (Ref 10, 29). However, determining the density of the films within the scope of this study is challenging due to the abrasive nature of the PAD process and the predominantly closed-porosity character of the films, which prevents meaningful density measurements.

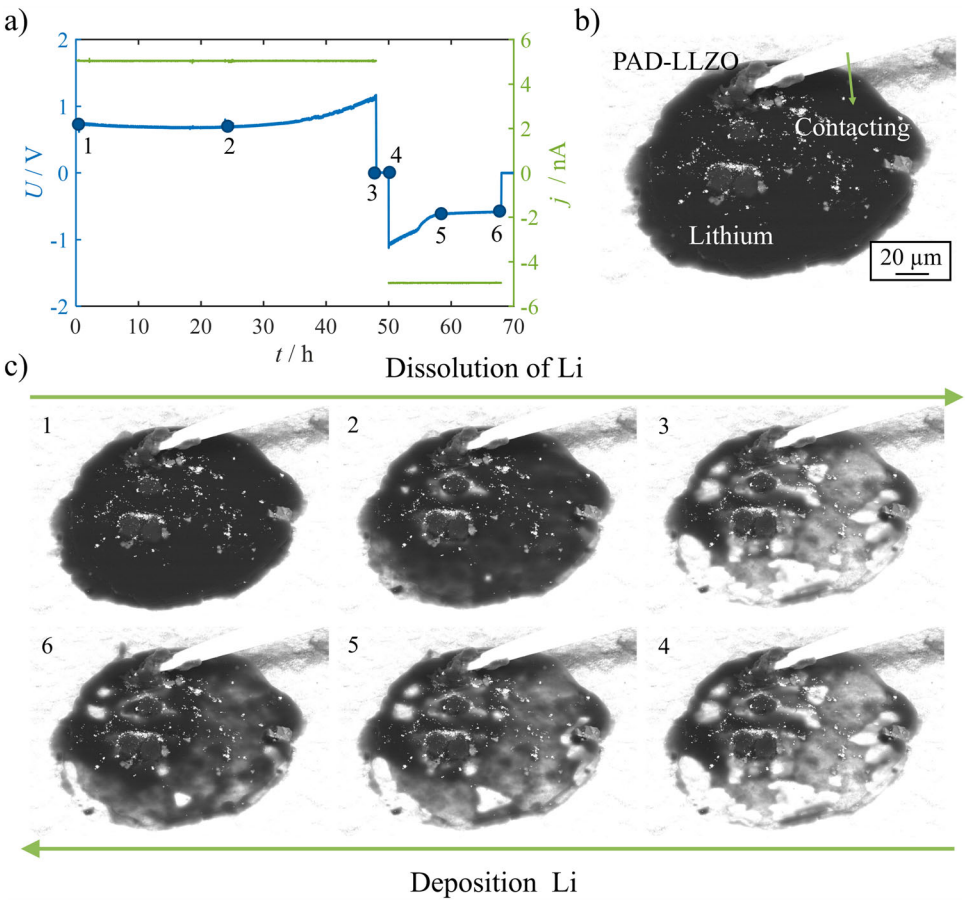

Fig. 1 Operando SEM observation of lithium dissolution and deposition performed on an as-deposited PAD-LLZO film: (a) current-voltage curve during lithium dissolution and deposition, (b) overview SEM image of the investigated sample, and (c) selection of SEM images during lithium dissolution and deposition at 1 BOL, 2 during dissolution, 3 after dissolution, 4 before deposition, 5 during deposition, and 6 after deposition. The experiment was conducted at room temperature with no external pressure applied

In summary, it can be concluded that lithium ions can be transported reversibly through a PAD-LLZO film. Therefore, we consider PAD-LLZO films as suitable for use as separator electrolyte layer in SSB cells.

The result of the electrochemical characterization with respect to the activation energy E_A of the ion transport via temperature-dependent measurements and electronic conductivity of an as-deposited PAD-LLZO films is displayed in Fig. 2. Figure 2(a) shows the value for E_A with the corresponding EIS spectra shown in Fig. S1(a) and (b) in the supporting information.

An activation energy E_A of 0.74 eV with an effective conductivity of $\sigma_{\text{eff,70 °C}} = 7.5{\cdot}10^{-7}$ S cm^{-1} at 70 °C is derived. Figure 2(b) shows the results of the Hebb-Wagner polarization experiment for another PAD-LLZO film. At 70 °C, an electronic conductivity of $\sigma_{\text{el,eff,20 °C}} = 6.1{\cdot}10^{-10}$ S cm^{-1} was obtained. However, the curve suggests that even lower values would be achieved with longer polarization times, so the value determined should be regarded as an upper limit. $\sigma_{\text{eff,70 °C}} = 4.4{\cdot}10^{-7}$ S cm^{-1} for the same sample was obtained with EIS analysis (cf. Fig. S1c). Consequently, the electronic conductivity is three orders of magnitude lower than the effective conductivity measured with EIS, suggesting that ionic conduction dominates with an electronic transference number of $t_{\text{electron}} = 2{\cdot}10^{-3}$.

The measurements to determine the critical current density j_{CCD} conducted on a further as-deposited PAD-LLZO film are shown in Fig. 3(a). The data recorded during the initial lithium electrodeposition can be found in Fig. S2 in the supporting information. For the as-deposited PAD-LLZO film, a j_{CCD} of 0.41 mA cm^{-2} is determined at 70 °C. The corresponding overvoltage during cycling increases from 0.6 V at 0.10 mA cm^{-2} to more than 2.3 V at the CCD value of 0.41 mA cm^{-2}.

EIS spectra measured during the determination of the CCD are shown in Fig. 3(b). Each spectrum consists of a single depressed semicircle. After cycling at 0.61 mA cm^{-2} (5), the EIS spectrum shows a strong decrease of the overall resistance. Despite the significant decline of the real part of the impedance, it remains at approximately 1.4 kΩ cm^2 at low frequencies, while a depressed semicircle can be observed. It is also noteworthy that, although a decrease in impedance would be expected after cycling at 0.41 mA cm^{-2} based on the data gathered during the CCD determination, a decrease is only observed after 0.61 mA cm^{-2}. This behavior may be attributed to dendrite growth occurring only in a portion of the film—

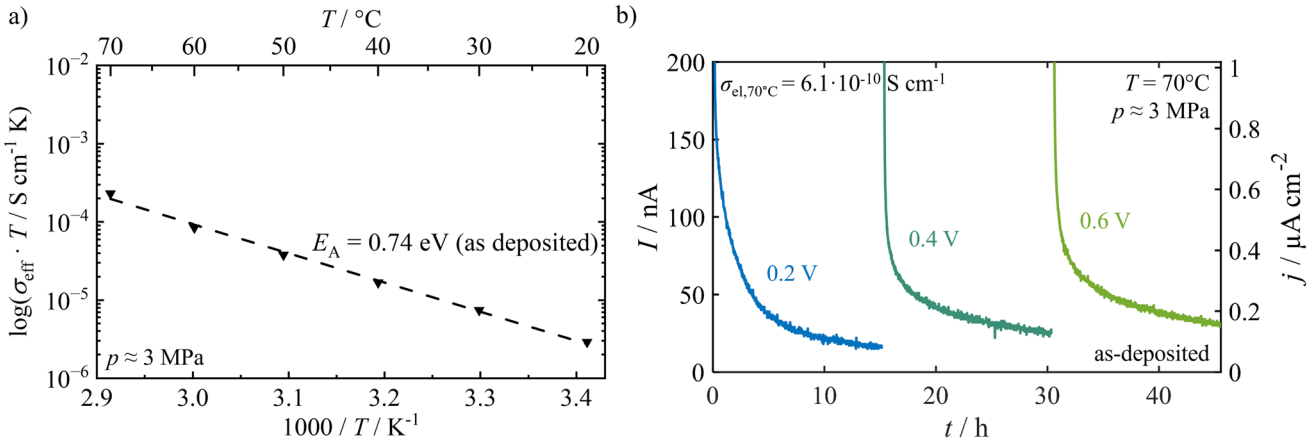

Fig. 2 Electrochemical characterization of the conductive properties of as-deposited PAD-LLZO films in a Cu|Li|LLZO|Li|Cu cell setup: (a) Arrhenius plot of the effective conductivity to determine E_A, the corresponding EIS spectra are shown in Fig. S1 in the supporting information, and (b) Hebb-Wagner polarization measurements at various potentials performed at 70 °C. The applied external pressure throughout all characterizations steps was ~ 3 MPa

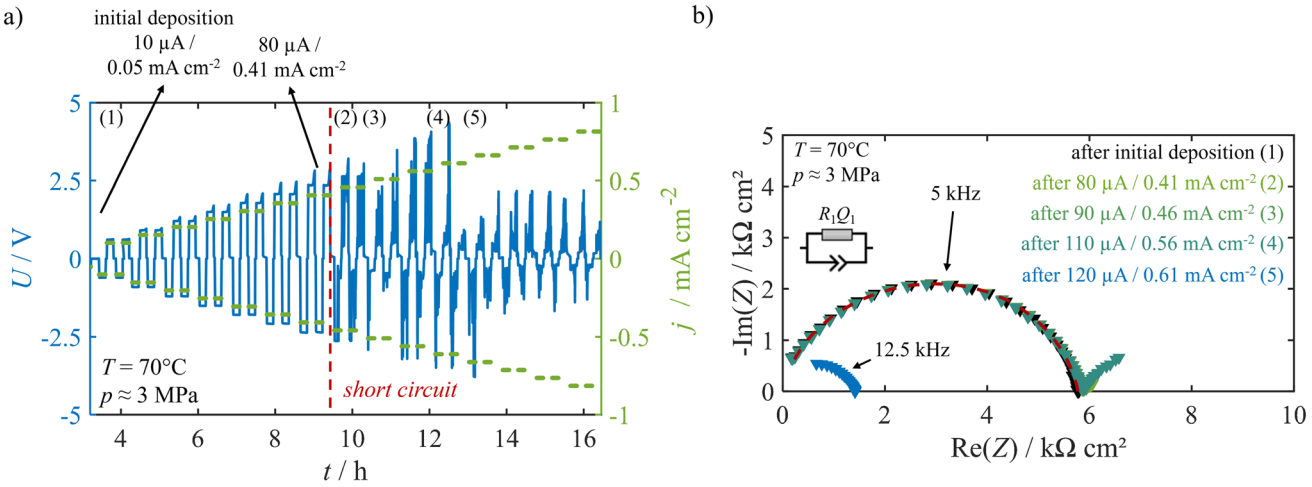

Fig. 3 Determination of the CCD of an as-deposited PAD-LLZO film in a Cu|Li|LLZO|Li|Cu cell setup: (a) stripping and plating of lithium with a CCD of j_{CCD} = 0.41 mA cm^{-2}, (b) EIS spectra measured during the CCD determination, points in time of measurement are indicated as (1) to (5) in (a). The applied external pressure throughout all characterization steps was ~ 3 MPa at 70 °C

likely near the electrode interface—effectively reducing the relevant electrode-to-electrode distance. In the literature, this phenomenon of an incomplete short is referred to as a partial or soft short circuit and has also been reported for LLZO pellet-based cells (Ref 30-36). A conceivable secondary scenario pertains to the penetration of thin filaments—exhibiting a resistance that is similar to that of the film itself—through the entirety of the film.

A quantitative analysis is performed for the EIS spectrum measured after the initial lithium electrodeposition (black, 1). From a physical point of view, a model structure of at least two non-ideal resistive-capacitive elements (RQ) should be assumed, representing the grain and the grain boundary contribution with a model structure of R_1Q_1-R_2Q_2. However, the shape of the spectrum suggests that one of these processes dominates the overall impedance of the cell or different processes with similar time constants are present, as evidenced by the presence of only one depressed semicircle. Consequently, the quantitative analysis is conducted with the model structure R_1Q_1, the results of which are shown as red dashed lines for the respective spectra. An overview of the fitted parameters is given in Table S2 in the supporting information. The determined resistance R_1 is 5.8·10^3 Ω cm^2 after the initial lithium electrodeposition. The corresponding capacitance is determined to be in the range of 10^{-9} F.

Similar results were achieved for the CCD determination of another as-deposited film. The data collected for this sample are shown in Fig. S3 in the supporting information.

Characterization of PAD-LLZO Films After Thermal Post-treatment

To improve the ionic conductivity, thermal post-treatment is commonly performed to induce relaxation of the lattice distortions and thus reduce microstrain in the film (Ref 20). Hanft et al. investigated the effect of thermal post-treatment at different temperatures on the electrochemical properties of PAD-LLZO films (Ref 14).

Their most significant findings in the context of this study are summarized in Fig. S4 in the supporting information. Hanft et al. showed that as a result of microstrain reduction the effective in-plane conductivity $\sigma_{\text{eff, ip}}$ can be increased. The most significant increase was achieved at an annealing temperature of 400 °C where $\sigma_{\text{eff,ip}}$ was increased from approximately 10^{-7} S cm^{-1} to approximately 10^{-5} S cm^{-1}. On the basis of this observation, T_{anneal} = 400 °C is often considered as the preferred annealing temperature for PAD-LLZO films, even though at higher annealing temperatures a further yet minor increase of $\sigma_{\text{eff, ip}}$ can be observed as a result of further microstrain reduction and grain growth (Ref 14). This assumption is made with the objective of limiting the energy requirements for sample preparation and maximizing the advantage of PAD as a fabrication process (Ref 11, 15).

In line with these previous findings, a PAD-LLZO film annealed at 400 °C for 1 h was electrochemically characterized to further investigate the challenges associated with the cycling stability. SEM images comparing the microstructure of as-deposited PAD-LLZO films and films annealed at different temperatures up to 700 °C can be found in the study of Hanft et al. (Ref 14). Figure 4 shows the activation energies E_A and the measurement of the electronic conductivity determined by Hebb-Wagner polarization. Once again, the measurements were conducted on two separate post-treated PAD-LLZO films.

Figure 4(a) shows the activation energies E_A of a first PAD-LLZO film annealed at 400 °C for 1 h in comparison with the data obtained for the as-deposited sample (c.f. Fig. 2(a). The corresponding EIS spectra can be found in Fig. S1 and S5 in the supporting information. After annealing at 400 °C, E_A was found to be decreased to 0.54 eV with an effective conductivity of $\sigma_{\text{eff,70 °C}}$ = 1.6·10^{-5} S cm^{-1}. The electronic conductivity of another PAD-LLZO film annealed at 400 °C for 1 h was determined to be $\sigma_{\text{el, eff, 70 °C}}$ = 3.8·10^{-9} S cm^{-1} at 70 °C (cf. Fig. 4b). Once again, the trajectory of the curve suggests that even lower values would be obtained if the polarization time would have been extended. Consequently, the determined value is regarded as an upper limit. The effective conductivity obtained through EIS analysis for the same sample is $\sigma_{\text{eff, 70 °C}}$ = 9.7·10^{-6} S cm^{-1} (cf. Fig. S5**c**) leading to an electronic transference number of t_{electron} = 4·10^{-4}. At first glance, this increase in ionic conductivity and decrease of E_A seems promising, especially since the ionic transfer number t_{ion} remains at close to 1.

The critical current densities of PAD-LLZO films annealed at 400 °C for 1 h were determined for a series of samples. A summary of the collected results is provided in Table S4 in the Supporting Information, while data for a representative sample are shown in Fig. 5(a).

Already at a low current density of only 0.05 mA cm^{-2}, a potential drop can be observed during the initial lithium electrodeposition within the first two hours. The overvoltage drops from − 0.03 V at 1.1 h to − 0.002 V at 2.1 h.

The EIS spectra measured during the CCD determination are shown in Fig. 5(c). The spectra at BOL (black) and

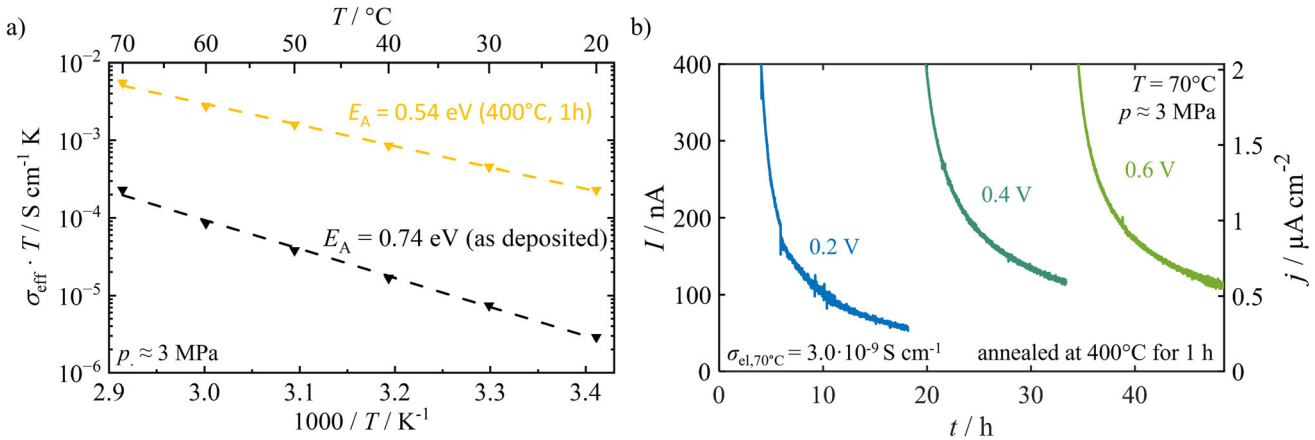

Fig. 4 Electrochemical characterization of PAD-LLZO films annealed at 400 °C for 1 h in a Cu|LLZO|Li|Cu cell setup: a) Arrhenius plot of the effective conductivity to determine E_A, the corresponding EIS spectra are shown in Fig. S3 in the supporting information, and b) Hebb-Wagner polarization measurements at various potentials performed at 70 °C. The applied external pressure throughout all characterization steps was ~ 3 MPa

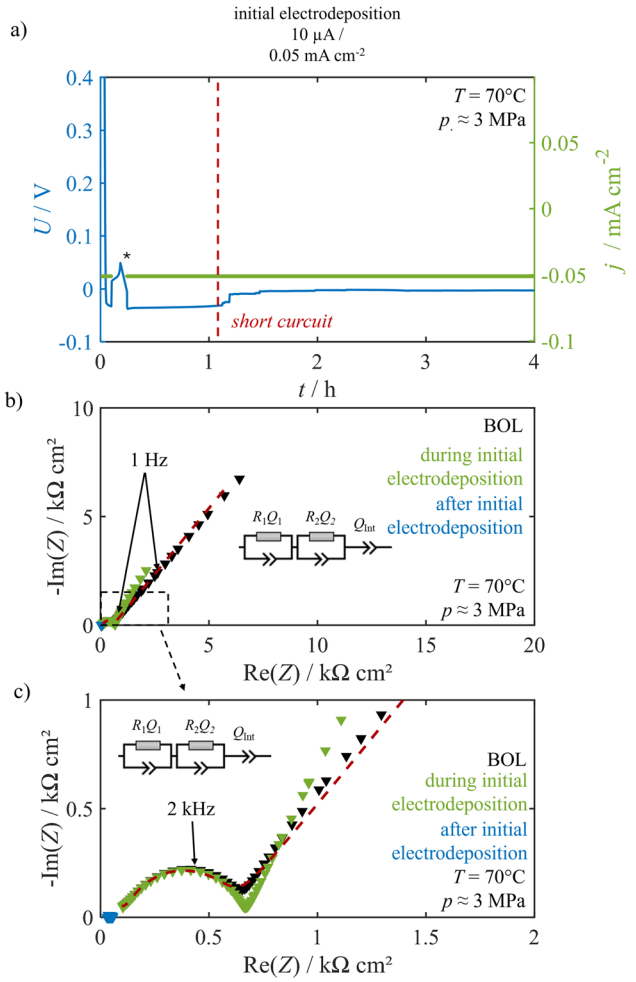

Fig. 5 Electrochemical characterization of a PAD-LLZO film annealed at 400 °C for 1 h in a Cu|LLZO|Li|Cu cell: a) initial lithium electrodeposition with a current density of j = 0.05 mA cm^{-2}, c) and d) EIS spectra measured after cell assembly (BOL, black), during initial lithium electrodeposition (green, marked with * in b)) and after the initial lithium electrodeposition was finished (blue). The applied external pressure throughout all characterization steps was ~ 3 MPa, and the temperature was kept at 70 °C

during the initial lithium electrodeposition (green) seem to consist of only one semicircle with an increasing imaginary part at low frequency. However, at high frequencies, the indication of a second semicircle can be observed, which becomes more apparent at lower temperatures (cf. Fig. S5b). For the spectra measured after the initial lithium electrodeposition, only a real part of the impedance can be observed.

A qualitative analysis is performed for the EIS spectra measured before the initial lithium electrodeposition (black). In comparison with the as-deposited sample, an additional semicircle appears at high frequencies in the EIS spectra, which becomes more pronounced at lower temperatures (cf. Fig. S5b). Additionally, in the Cu|LLZO|Li cell setup, a blocking electrode is present, which is assumed to be responsible for the increasing imaginary part at low frequency. Consequently, an equivalent circuit model extended with a second R_2Q_2 element and Q_{Int} representing the blocking contribution of the cell at the Cu|LLZO is found to fit the EIS data. The results of the fit are displayed as red dotted line, and an overview of the fit parameters can be found in Table S3 in the supporting information. The resistances for the RQ elements are 114 Ω cm^2 and 4.6·10^2 Ω cm^2, respectively, with corresponding capacitances of 10^{-10} F and 10^{-8} F.

These results raise the question of what occurs during thermal annealing. Although the ionic conductivity increases, it appears that the reduction in film stress and microstrain negatively affects the cycling performance of PAD-LLZO films. In particular, the vulnerability of the films to dendrite growth seems to increase.

Microstructural Challenges of PAD-LLZO Films for SSBs Applications

PAD-LLZO Film in the As-Deposited State

The reversible lithium transport utilizing a PAD-LLZO film as an SE layer has been observed at ambient temperatures (c.f. Fig. 1). At 70 °C, current densities of up to 0.41 mA cm^{-2} are achieved in a symmetrical cell setup (c.f. Fig. 3). To the best of our knowledge, such observations have not been demonstrated for any other film fabrication process reported in the literature, particularly for films with thicknesses in the 10-µm range and below 50 µm. The data collected here suggest that PAD-LLZO films might be suitable for use as electrolyte layers in SSBs as previously demonstrated in the literature—once the ionic conductivity could be further increased. In the as-deposited state, the ionic conductivity is still too low, being 3 orders of magnitude lower than the minimum requirement of 10^{-4} S cm^{-1}.

In view of these results, the electrochemical properties of the as-deposited PAD-LLZO film need to be improved to be sufficient for application in SSBs. While it can be assumed that the film is mostly ionically conducting (transfer number of $t_{electron}$ = 2·10^{-3}), both effective conductivity ($\sigma_{eff,\ 70\ °C}$ = 6.7·10^{-7} S cm^{-1}) and E_A (0.74 eV) are inferior compared to the values reported in the literature for sintered bulk materials, which typically range from 0.2 eV to 0.5 eV for E_A and 10^{-3} S cm^{-1} to 10^{-5} S cm^{-1} for σ (Ref 4, 7). These limitations result in excessive overvoltage during cycling restricting the applicability of the layers in SSBs. In addition, PAD-LLZO films exhibit somewhat higher electronic conductivities compared to their sintered counterparts. Usually, ratios in ionic and electronic conductivity for LLZO are found to be in the

range of 4 to 7 orders of magnitude with transfer numbers of $t_{electron} < 10^{-4}$ (Ref 7, 37, 38).

In accordance with the data reported in the literature, we attribute these observations to the distinctive microstructure of PAD-LLZO films. As described previously, PAD films are of a nanocrystalline structure with a significantly higher number of grain boundaries compared to bulk materials. In addition, the PAD deposition mechanism leads to microstrain and stresses within the films (Ref 14, 39, 40). This microstructure—in particular the nanocrystalline structure and microstrain—influences the cell performance in two ways. First, the impedance is dominated by the grain boundary contribution as indicated by the capacitance in the range of 10^{-9} F obtained for the *RQ*-element which corresponds to ionic transport across grain boundaries in the literature (Ref 41-43). We attribute this to an increased volume fraction of grain boundaries and lattice distortions that are predominantly localized there. As a result, the ionic charge carrier mobility at the grain boundaries is significantly lower than within the grains themselves, leading to high resistance to ion diffusion and thus to a lower ionic conductivity.

Second, the increased grain boundary volume fraction may account for the observed increased electronic conductivity. Grain boundaries may be associated with local disorder in the chemical bonds of LLZO and therefore are expected to lead to deteriorated electrochemical properties of the electrolyte, i.e., decreased ionic and increased electronic transport. According to literature, the band gap for electronic conduction at LLZO grain boundaries (1 to 3 eV) is narrower than in the bulk material (6 eV) (Ref 30). Therefore, the higher volume fraction of grain boundaries and near-boundary regions in PAD films compared to bulk materials may facilitate electron transport, ultimately contributing to the observed increased electronic conductivity.

Other studies utilizing PAD-LLZO films with a cell setup containing a reversible lithium electrode report similar values of 0.50 eV and 0.65 eV for E_A with conductivities of around

10^{-7} S cm^{-1} at a temperature of 70 °C confirming the results of this study (Ref 11, 15). In essence, PAD-LLZO films in the as-deposited state exhibit reduced ionic conductivity and increased electronic conductivity as a result of their microstructural features.

Overall, these findings prove that the microstructure of PAD-LLZO films plays a crucial role in determining their electrochemical performance. This aligns with results previously reported in the literature for LLZO and other materials processed via PAD (Ref 14, 20).

PAD-LLZO Film Annealed at 400 °C for 1 h

After annealing the PAD-LLZO film at 400 °C for 1 h, the effective conductivity increased by nearly two orders of magnitude to $\sigma_{eff,70\ °C} = 1.6{\cdot}10^{-5}$ S cm^{-1}, while E_A decreased to 0.54 eV in contrast to the as-deposited film. The ionic conduction remains to be dominant with an electronic transference number of $t_{electron} = 4{\cdot}10^{-4}$, as the measured electronic conductivity is approximately four orders of magnitude lower than the σ_{eff} determined by EIS analysis. Interestingly, the ionic conductivity increases by almost two orders of magnitude, while the electronic conductivity exhibits only a marginal increase by a factor of 4 in comparison with the as-deposited film.

Based on the results reported by Hanft et al., this increase in ionic conductivity is attributed to the recovery of an unstrained crystalline lattice in the grain. As shown in Fig. S4a and b, the crystallite size remains constant up to an annealing temperature of 400 °C, while the microstrain is reduced by roughly a factor of two. Consequently, it can be assumed that the volume fraction of grain boundaries remains essentially unchanged and therefore does not contribute to the observed increase in ionic conductivity. For a more detailed analysis of the underlying mechanism of the annealing effect, the authors refer the reader to the study of Exner et al. (Ref 20). Taken together, these results suggest that in isolated PAD-LLZO films, ionic conductivity is impaired by microstrain, while electronic conductivity appears to be less affected by this phenomenon.

The effect of thermal post-treatment can also be observed for the impedance of the PAD-LLZO films. After annealing, a second distinct process becomes visible at high frequencies. In the literature, the contribution at high frequencies is usually assigned to the ionic transport within the grain while the contribution at intermediate frequencies is assigned to the (more resistive) grain boundary contributions (Ref 41, 42, 44-46). Under this assumption, we conclude that annealing enhances charge-transfer processes across grain boundaries due to the reestablishment of an undistorted lattice and therefore reduced microstrain, as evidenced by the approximately one-order-of-magnitude decrease in the resistance associated with the intermediate-frequency contribution.

Despite the significant improvement in ionic conductivity after annealing, the achieved values for σ_{eff} still fall short of the minimum requirement of 10^{-4} S cm^{-1} for practical solid-state battery operation. This limitation is likely linked to the high grain-boundary volume fraction in PAD-LLZO films, which results from the nanocrystalline microstructure and imposes a substantial resistive contribution even after microstrain relaxation.

In contrast to the improved conductivity, the cycling stability of PAD-LLZO films is not enhanced by thermal

annealing. For the post-treated film, a short circuit indicated by the potential drop after approximately 1 h occurred already during the initial lithium electrodeposition at a current density of 0.05 mA cm^{-2}. This represents a drastic decrease in the CCD compared to the as-deposited film. This agrees well with the results obtained from the EIS analyses and cycling experiments conducted for a series of other PAD-LLZO films investigated after a thermal annealing at 400 °C for 1 h. (c.f. Table S4). This raises the question of what happens during annealing that leads to the degradation of cycling stability.

Susceptibility of PAD-LLZO Films to Lithium-Filament Formation

Ideally, the improved ionic conductivity would reduce the overvoltage during cycling and lead to an increase in CCD. However, an opposite trend is observed in this study. The data of the PAD-LLZO films annealed at 400 °C for 1 h suggest that the reduction in film stress and the relaxation of lattice deformation may facilitate lithium penetration through the PAD-LLZO film during cycling, resulting in short circuits at relatively low current densities.

In order to increase the CCD of PAD-LLZO films while maintaining high ionic conductivity, the failure mechanism during cycling has to be understood. Contrary to the classical dendrite growth mechanism observed in LIB with liquid electrolytes (in the literature referred to as mode 1 (Ref 47)), recent studies suggest that the grain boundaries within PAD-LLZO films play an important role in the lithium dendrite or so-called lithium "filament" formation during cycling (Ref 30, 48). It has been proposed that grain boundaries may possess a smaller bandgap compared to the bulk material. Therefore, they can show enhanced electronic conductivity and can trap electrons if they are close to a plating lithium electrode. This may result in local overvoltage that exceeds the threshold required for the electrochemical reduction of lithium ions. As a result, metallic lithium filaments grow along the grain boundaries progressing through the separator layer during cycling. In the literature, this second failure mechanism is referred to as mode 2 (Ref 47).

This leads to the assumption that an increased grain boundary volume fraction will promote the growth of lithium filaments. Looking at the microstructure of PAD films with typical grain sizes around some 10 nm, grain boundary volume fraction in PAD films is considerably higher compared to bulk materials or films with grain sizes in the µm range (Ref 39, 49). This may make PAD films particularly vulnerable to lithium-filament growth, leading to short circuits already at low current densities. This assumption is further supported by the results obtained and discussed in this study.

Assuming the validity of this specific failure mechanism, the electrochemical behavior observed in the cells characterized so far can be explained. The as-deposited PAD-LLZO films exhibit a pronounced drop in resistance at current densities above 0.41 mA cm^{-2}, although the real part of the impedance remains in the kΩ range even after this decrease (c.f. Fig. 3 and Fig. S2 in the supporting information). As already discussed earlier, this behavior might be attributed to localized filament growth in a section of the film—likely near the electrode interface—or full penetration of the film by highly resistive filaments (Ref 30-36). In contrast, the PAD-LLZO film annealed at 400 °C exhibits a stepwise decrease in overvoltage during the initial stages of the lithium electrodeposition (j = 0.05 mA cm^{-2}), ultimately resulting in a complete short circuit which is also supported by the EIS analyses (c.f. Fig. 5 and Table S4 in the supporting information). This suggests that, in this case, lithium filaments penetrate the entire film.

This leads to the conclusion that filament formation in the PAD-LLZO film annealed at 400 °C occurs at lower current densities compared to the as-deposited film, despite the similar microstructures in terms of grain sizes, which can be assumed as a result of the data by Hanft et al. (c.f. Fig. S4a) (Ref 14). We speculate that this discrepancy may be attributed to internal compressive film stresses—particularly at grain boundaries—present in the as-deposited state, phenomena which have been characterized in the literature (Ref 14, 40). As a result, the grain boundary pathways for filament propagation may be compromised for the as-deposited samples, while for the annealed samples those pathways are more accessible as a result of reduced stresses. For a more detailed analysis of the effect of annealing on compressive stresses in PAD films, the reader is referred to our previous study by Paulus et al. (Ref 40).

This speculation aligns with findings by Fincher et al., who demonstrated that lithium dendrite propagation in LLZO is strongly influenced by mechanical stress (Ref 50). In their study, the application of uniaxial pressure led to dendrite growth preferentially along the loading direction. They specify a critical stress of approximately 150 MPa, while the intrinsic compressive stress of PAD films is usually in the GPa range (Ref 40, 50-53). A thermal post-treatment relieves these compressive stresses, therefore facilitating filament growth along the grain boundaries in the annealed film.

In the light of our observations and previous reports, we conclude that PAD-LLZO films annealed at 400 °C cannot be used as separator layers in SSBs, owing to their nanocrystalline microstructure. To further enhance the resistance of the films against lithium-filament growth and improve the CCD, while simultaneously ensuring

sufficiently high ionic conductivity, a suitable post-treatment method has yet to be identified. Such a method should aim to modify the characteristic microstructure of PAD-LLZO films with respect to the grain size and the grain-boundary volume fraction. Adjusting these parameters may not only improve the robustness against filament penetration but may also further increase the ionic conductivity and reduce the electronic conductivity by reducing the proportion of resistive grain boundaries, helping to approach the minimum requirement of 10^{-4} S cm^{-1} and further reduce $t_{electron}$.

Modification of the Microstructure of PAD-LLZO Films

To modify the microstructure of PAD-LLZO films, two strategies may be considered. In a straightforward approach, the grain size is increased in the film to reduce the grain boundary volume fraction, thereby shifting the microstructure toward that of dense ceramic pellets. Alternatively, the grain boundaries themselves could be modified to minimize their negative impact on the stability against lithium-filament formation during cycling.

In an attempt to reduce the volume fraction of grain boundaries within the PAD-LLZO films, temperature and dwell time of the thermal annealing step were increased according to the results of Hanft et al. (c.f. Fig. S4c). They showed that temperatures above 500 °C yield increased crystallite sizes in PAD-LLZO films (green markers) (Ref 14). To apply these findings to the present study, we assume that in PAD films each grain consists only of a single domain, so that the terms grain size and crystallite size can be used synonymously (Ref 39, 49). Accordingly, it is assumed that with increasing crystallite sizes, the volume fraction of grain boundaries is reduced.

Based on the data shown in Fig. S4(c), a post-treatment temperature of 700 °C was selected for the initial investigation. This temperature is expected to promote sufficient grain growth while avoiding excessively high temperatures that could lead to lithium loss, a phenomenon known to occur at elevated temperatures (Ref 54, 55). To allow for sufficient grain growth, a dwell time of 48 h was chosen for an initial investigation. The extended dwell time at this temperature is anticipated to promote diffusion-driven grain growth and to reduce the gap between the grain sizes of PAD-LLZO films and those observed in sintered bulk reference materials as far as possible without requiring higher temperatures.

Doing so, LLZO powder, an as-deposited PAD-LLZO film, a PAD-LLZO film annealed at 400 °C for 1 h, and a PAD-LLZO film annealed at 700 °C for 48 h were characterized using XRD. The results are shown in Fig. 6. To avoid distorting reflections from the substrate in the diffraction patterns, the films for XRD were deposited on silicon wafers with a (911) orientation.

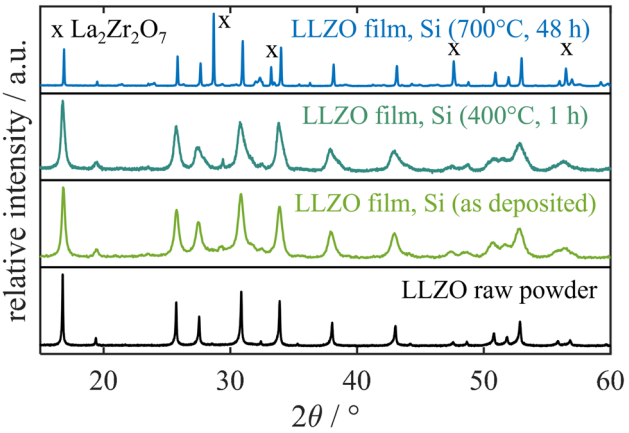

Fig. 6 XRD patterns of LLZO powder (black), as-deposited PAD-LLZO film (light green), PAD-LLZO film annealed at 400 °C for 1 h (dark green), and PAD-LLZO film annealed at 700 °C for 48 h (blue)

Table 1 Crystallite size D and microstrain ε_0 of the samples analyzed in Fig. 6 determined via rietveld refinement of the diffraction patterns

	Raw powder	As-deposited	400 °C, 1 h	700 °C, 48 h
D/nm	> 500	38	34	194
ε_0/%	0.02	1.05	1.58	0.16

The position of the reflections in diffraction patterns of all samples indicates the desired cubic garnet-type structure characteristic for LLZO. In addition, the pattern of the film annealed at 700 °C for 48 h also shows reflections of the pyrochlore phase $La_2Zr_2O_7$ (marked with x). This may be due to lithium loss during the post-treatment for 48 h at 700 °C, which is a phenomenon known to occur at elevated temperatures (Ref 54-56). The diffraction patterns of the powder and of the film annealed at 700 °C for 48 h show narrow reflections, whereas for the as-deposited film and the film annealed at 400 °C for 1 h broad reflections can be observed. Typically, broader reflections are due to a smaller grain size and the presence of lattice strain, i.e., mechanical stress inhomogeneities, which are very common phenomena for films deposited by PAD (Ref 20, 40, 57, 58). The narrow reflections observed for the PAD-LLZO film annealed at 700 °C indicate crystallite growth during annealing.

In order to obtain further information regarding the crystallite size denoted as D and microstrain denoted as ε_0, Rietveld refinement was performed. The results of this refinement are shown in Table 1.

The crystallite size D of the raw powder is > 500 nm, which corresponds to the upper resolution limit of resolution. After deposition, the crystallite size decreases to

Table 2 Overview on the key findings of this study in terms of microstructural and electrochemical properties of the different sample types investigated

	$f_{V,\text{as-deposited}}$, a.u.	$f_{\varepsilon 0,\text{as-deposited}}$, a.u.	$\sigma_{\text{eff, 70 °C}}$, S cm^{-1}	$\sigma_{\text{el, 70 °C}}$, S cm^{-1}	$j_{\text{CCD, 70 °C}}$, mA cm^{-2}
As-deposited	1	1	$7.5 \cdot 10^{-7}$	$6.1 \cdot 10^{-10}$	0.41
400 °C, 1 h	1 (Ref 14)	0.47 (Ref 14)	$1.6 \cdot 10^{-5}$	$3.8 \cdot 10^{-9}$	0.05
700 °C, 48 h	130	0.15	…	…	…

*The microstructural properties are presented as dimensionless relative volume factor $f_{\text{V,as-deposited}}$, referenced respect to the as-deposited state, and relative microstrain factor $f_{\varepsilon 0,\text{as-deposited}}$, likewise referenced to the as-deposited state

38 nm, and after annealing at 400 °C for 1 h, it remains essentially unchanged at 34 nm. After being annealed at 700 °C for 48 h, the crystallite size increased significantly to 194 nm. The microstrain ε_0 is determined to be 0.02 % for the raw powder, 1.05 % for the as-deposited sample, 1.58 % after annealing at 400 °C for 1 h, and 0.16 % after annealing at 700 °C for 48 h.

Since the grain volume scales cubically with the crystallite size D, the heat treatment leads to an increase in grain volume for the PAD-LLZO film annealed at 700 °C for 48 h by a factor of $\sim$ 130—(194 nm/38 nm)^3—in relation to the as-deposited state. With regard to the grain boundary volume fraction, the ratio of grain boundary volume to grain volume reduces from 15.0 % (as-deposited) to 3.1 % (after annealing at 700 °C), when assuming a grain boundary "thickness" of 1 nm. An assumption consistent with Liu et al., who report values below 1.5 nm for LLZO (Ref 30). We conclude that the microstructure with respect to the grain size of PAD-LLZO films can be tuned by modifying the post-treatment conditions. It should be noted that, following a proof-of-concept regarding the effect of the post-treatment on cycling stability, further studies should focus on optimizing the post-treatment conditions. The dwell time and potentially also the annealing temperature should be reduced in order to lower energy consumption and preserve the intrinsic processing advantages of PAD. Furthermore, the formation conditions and the influence of the observed $La_2Zr_2O_7$ pyrochlore phase on the electrochemical properties must be considered. This is particularly important, as this phase is well known to detrimentally affect electrochemical performance due to its insulating character (Ref 56).

In terms of microstrain ε_0, the results for the raw powder, the as-deposited film, and the film annealed at 700 °C for 48 h are similar to values previously reported in literature (Ref 14, 57). For the raw powder, a low ε_0 of 0.02 % is determined, which increases to 1.05 % for the as-deposited film as a result of lattice distortions. After annealing at 700 °C for 48 h, ε_0 is significantly reduced to 0.16 %, which can be attributed to the recovery of an undistorted lattice.

However, ε_0 determined for the PAD-LLZO film annealed at 400 °C for 1 h deviates from the literature. Based on literature data, one would expect a value lower than that of the as-deposited sample, which is also supported by the electrochemical behavior discussed above. In contrast, an increase in microstrain is observed after annealing at 400 °C. At present, no conclusive explanation for this deviation can be given, and further investigations are required to clarify this behavior.

To summarize the findings of this study, the key properties of the investigated samples are presented once again in Table 2. Therefore, the microstructural properties are presented as dimensionless relative volume factor $f_{\text{V,as-deposited}}$, referenced with respect to the as-deposited state, and relative microstrain factor $f_{\varepsilon 0,\text{as-deposited}}$, likewise referenced to the as-deposited state. It should be noted that the factors shown for the PAD-LLZO film annealed at 400 °C were determined with respect to the data reported by Hanft et al. to allow for a meaningful comparison (Ref 14). The electrochemical properties measured at 70 °C are represented by the effective ionic conductivity $\sigma_{\text{eff, 70 °C}}$, the electronic conductivity $\sigma_{\text{el, 70 °C}}$, and the CCD $j_{\text{CCD, 70 °C}}$.

Conclusions

Identifying a suitable processing method to fabricate dense LLZO electrolyte layers remains one of the key challenges for their implementation in SSBs for commercial applications. In the present study, the potential for overcoming this challenge using the powder aerosol deposition method (PAD)—a room temperature deposition method—was examined. Using operando SEM, it was demonstrated that PAD-LLZO films can be utilized for the reversible transport of lithium, however, still at high overvoltage. In addition, current densities of up to 0.41 mA cm^{-2} were achieved with no temperature treatment applied. To further improve the cycling properties, a thermal post-treatment at mild conditions (400 °C for 1 h) was investigated. Following this thermal post-treatment, a critical current density of only 0.05 mA cm^{-2} was observed. It is assumed

that the reduction in compressive film stresses and microstrain resulted in a deterioration of the cycling stability in terms of CCD. This hypothesis can be justified by the unique nanocrystalline microstructure of PAD films with small crystallite sizes in the 10-nm range. The resulting large volume fraction of grain boundaries, in contrast to bulk LLZO, may accelerate lithium-filament formation during cycling. Considering these findings, a possible strategy to improve the resistance against filament formation and further increase ionic conductivity through the reduction of grain boundary volume fraction was proposed. Initial results indicate that increasing the annealing temperature and dwell time leads to a significant increase in grain size that reduces the grain boundary volume fraction within the film. Accordingly, it is suggested that in a primary effort future studies should focus on evaluating the electrochemical properties of PAD-LLZO films subjected to the adapted post-treatment.

Supplementary Information The online version contains supplementary material available at https://doi.org/10.1007/s11666-026-02240-3.

Acknowledgments Support by the BayBatt Cell Technology Center is gratefully acknowledged, funded by the Deutsche Forschungsgemeinschaft (DFG, German Research Foundation)—INST 91/452-1 LAGG. The authors thank the Bavarian Polymer Institute (BPI, KeyLab Electron and Optical Microscopy) for providing the SEM equipment. Furthermore, we thank the Department of Metal and Alloys (Prof. U. Glatzel) for providing the equipment for XRD measurements.

Author Contribution L.H. was responsible for film fabrication as well as sample and cell preparation, performed the electrochemical characterization experiments, and evaluated the generated data. L.H., T.F., and M.L. evaluated and discussed the data retrieved through electrochemical characterization. L.H. and D.P. performed the evaluation of the XRD data. S.L. was responsible for conducting the operando SEM observation. D.K., R.Moe., D.S.K., J. J. as well as R.M. supervised the work. L.H., D.S.K., and R.M. prepared the submitted manuscript. All authors discussed the results received, have read, and agreed to the published version of the manuscript.

Funding Open Access funding enabled and organized by Projekt DEAL. The authors would like to thank the German Federal Ministry of Education and Research (BMBF) within the framework of the FestBatt2 cluster (BMBF grant 03XP0441A and 03XP0441C) and the Bavarian Center for Battery Technology (BayBatt) for funding this research work. T.F. and J.J. acknowledge financial support from the German Federal Ministry of Education and Research (BMBF) under the project "CatSE 2" (grant identifier 03XP0510E).

References

1. A. Manthiram, X. Yu, and S. Wang, Lithium Battery Chemistries Enabled by Solid-State Electrolytes, *Nat. Rev. Mater.*, 2017, **2**, p 16103. https://doi.org/10.1038/natrevmats.2016.103
2. T. Ye, L. Li, and Y. Zhang, Recent Progress in Solid Electrolytes for Energy Storage Devices, *Adv. Funct. Mater.*, 2020, **30**, p 2000077. https://doi.org/10.1002/adfm.202000077
3. Z. Wu, Z. Xie, A. Yoshida, Z. Wang, X. Hao, A. Abudula, and G. Guan, Utmost Limits of Various Solid Electrolytes in All-solid-state Lithium Batteries: A Critical Review, *Renew. Sustain. Energy Rev.*, 2019, **109**, p 367-385. https://doi.org/10.1016/j.rser.2019.04.035
4. Y. Wang, Z. Chen, K. Jiang, Z. Shen, S. Passerini, and M. Chen, Accelerating the Development of LLZO in solid-state Batteries Toward Commercialization: A Comprehensive Review, *Small*, 2024, **20**, p e2402035. https://doi.org/10.1002/smll.202402035
5. Q. Liu, Z. Geng, C. Han, Y. Fu, S. Li, Y. He, F. Kang, and B. Li, Challenges and Perspectives of Garnet Solid Electrolytes for All solid-state Lithium Batteries, *J. Power. Sources*, 2018, **389**, p 120-134. https://doi.org/10.1016/j.jpowsour.2018.04.019
6. X. Shen, Q. Zhang, T. Ning, T. Liu, Y. Luo, X. He, Z. Luo, and A. Lu, Critical Challenges and Progress of Solid Garnet Electrolytes for All-solid-state Batteries, *Mater. Today Chem.*, 2020, **18**, p 100368. https://doi.org/10.1016/j.mtchem.2020.100368
7. J.-F. Wu, E.-Y. Chen, Y. Yu, L. Liu, Y. Wu, W.K. Pang, V.K. Peterson, and X. Guo, Gallium-Doped $Li_7La_3Zr_2O_{12}$ garnet-type Electrolytes with High Lithium-Ion Conductivity, *ACS Appl. Mater. Interfaces*, 2017, **9**, p 1542-1552. https://doi.org/10.1021/acsami.6b13902
8. F. Flatscher, M. Philipp, S. Ganschow, H.M.R. Wilkening, and D. Rettenwander, The Natural Critical Current Density Limit for $Li_7La_3Zr_2O_{12}$ Garnets, *J. Mater. Chem. A*, 2020, **8**, p 15782-15788. https://doi.org/10.1039/c9ta14177d
9. S. Randau, D.A. Weber, O. Kötz, R. Koerver, P. Braun, A. Weber, E. Ivers-Tiffée, T. Adermann, J. Kulisch, W.G. Zeier, F.H. Richter, and J. Janek, Benchmarking the Performance of All-solid-state Lithium Batteries, *Nat. Energy*, 2020, **5**, p 259-270. https://doi.org/10.1038/s41560-020-0565-1
10. D. Hanft, J. Exner, M. Schubert, T. Stöcker, P. Fuierer, and R. Moos, An Overview of the Aerosol Deposition Method: Process Fundamentals and New Trends in Materials Applications, *J. Ceram. Sci. Technol.*, 2015, **6**, p 147-182. https://doi.org/10.4416/JCST2015-00018
11. T. Nazarenus, Y. Sun, J. Exner, J. Kita, and R. Moos, Powder Aerosol Deposition as a Method to Produce garnet-type Solid Ceramic Electrolytes: A Study on Electrochemical Film Properties and Industrial Applications, *Energy Technol.*, 2021, **9**, p 2100211. https://doi.org/10.1002/ente.202100211
12. T. Nazarenus, J. Schneider, L. Hennerici, R. Moos, and J. Kita, Energy Estimation of the Post-treatment Process for Powder Aerosol Deposited Solid Electrolyte Films, *Funct. Mater. Lett.*,

2023, **16**, p 2350014. https://doi.org/10.1142/S1793604723500145
13. L. Hennerici, P. Ficht, M. Schamel, U. Mansfeld, M. Linz, D. Paulus, J. Kita, M.A. Danzer, and R. Moos, Lithium All-solid-state Batteries Fabricated at Room Temperature by the Powder Aerosol Deposition Method with garnet-type Electrolyte and Graded Composite Cathode, *Adv. Mater. Technol.*, 2024, **10**, p 2400745. https://doi.org/10.1002/admt.202400745
14. D. Hanft, J. Exner, and R. Moos, Thick-Films of garnet-type Lithium Ion Conductor Prepared by the Aerosol Deposition Method: the Role of Morphology and Annealing Treatment on the Ionic Conductivity, *J. Power. Sources*, 2017, **361**, p 61-69. https://doi.org/10.1016/j.jpowsour.2017.06.061
15. M. Hahn, D. Rosenbach, A. Krimalowski, T. Nazarenus, R. Moos, M. Thelakkat, and M.A. Danzer, Investigating Solid Polymer and Ceramic Electrolytes for Lithium-Ion Batteries by Means of an Extended Distribution of Relaxation Times analysis, *Electrochim. Acta*, 2020, **344**, p 136060. https://doi.org/10.1016/j.electacta.2020.136060
16. C.-W. Ahn, J.-J. Choi, J. Ryu, B.-D. Hahn, J.-W. Kim, W.-H. Yoon, J.-H. Choi, and D.-S. Park, Microstructure and Ionic Conductivity in $Li_7La_3Zr_2O_{12}$ Film Prepared by Aerosol Deposition Method, *J. Electrochem. Soc.*, 2015, **162**, p A60-A63. https://doi.org/10.1149/2.0411501jes
17. R. Inada, T. Okada, A. Bando, T. Tojo, and Y. Sakurai, Properties of Garnet-Type $Li_6La_3ZrTaO_{12}$ Solid Electrolyte Films Fabricated by Aerosol Deposition Method, *Prog. Nat. Sci. Mater. Int.*, 2017, **27**, p 350-355. https://doi.org/10.1016/j.pnsc.2017.06.002
18. J. Han, A. Vu, J.J. Kim, J. Gim, J.R. Croy, T.H. Lee, and E. Lee, Room-Temperature Fabrication of garnet-type Solid-Electrolyte: Optimizing Particle Size for High Ionic Conductivity, *Chem. Eng. J.*, 2024, **481**, p 148645. https://doi.org/10.1016/j.cej.2024.148645
19. S. Yu and D.J. Siegel, Grain Boundary Contributions to Li-Ion Transport in the Solid Electrolyte $Li_7La_3Zr_2O_{12}$ (LLZO), *Chem. Mater.*, 2017, **29**, p 9639-9647. https://doi.org/10.1021/acs.chemmater.7b02805
20. J. Exner, T. Nazarenus, D. Hanft, J. Kita, and R. Moos, What Happens during Thermal Post-treatment of Powder Aerosol Deposited Functional Ceramic Films? Explanations Based on an Experiment-Enhanced Literature Survey, *Adv. Mater.*, 2020, **32**, p e1908104. https://doi.org/10.1002/adma.201908104
21. M. Lebedev, J. Akedo, A. Iwata, S. Sugimoto and K. Inomata, NiZnCu Ferrite Thick Film with Nano Scale Crystallites Formed by the Aerosol Deposition Method, *J. Am. Ceram. Soc.*, 2004, **87**, p 1621-1624. https://doi.org/10.1111/j.1551-2916.2004.01621.x
22. N. Hoinkis, J. Schuhmacher, S. Leukel, C. Loho, A. Roters, F.H. Richter, and J. Janek, Particle Size-Dependent Degradation Kinetics of garnet-type $Li_{6.5}La_3Zr_{1.5}Ta_{0.5}O_{12}$ Solid Electrolyte Powders in Ambient Air, *J. Phys. Chem. C*, 2023, **127**, p 8320-8331. https://doi.org/10.1021/acs.jpcc.3c01027
23. D. Hanft, P. Glosse, S. Denneler, T. Berthold, M. Oomen, S. Kauffmann-Weiss, F. Weis, W. Häßler, B. Holzapfe,l and R. Moos, The Aerosol Deposition Method: A Modified Aerosol Generation Unit to Improve Coating Quality, *Materials*, 2018, **11**, p 9. https://doi.org/10.3390/ma11091572
24. D. Balzar and H. Ledbetter, Accurate Modeling of Size and Strain Broadening in the Rietveld Refinement: The "Double-Voigt" Approach, *Adv. X-ray Anal.*, 1994, **38**, p 397-404. https://doi.org/10.1154/S0376030800018048
25. D. Balzar and H. Ledbetter, Voigt-Function Modeling in Fourier analysis of Size- and Strain-Broadened X-ray Diffraction Peaks, *J. Appl. Crystallogr.*, 1993, **26**, p 97-103. https://doi.org/10.1107/S0021889892008987
26. M. Järvinen, Application of Symmetrized Harmonics Expansion to Correction of the Preferred Orientation Effect, *J. Appl. Crystallogr.*, 1993, **26**, p 525-531. https://doi.org/10.1107/S0021889893001219
27. D. Paulus, M. Linz, A.-L. Hansen, S. van Smaalen, R. Moos, A.S. Ulrich, and D. Schönauer-Kamin, Structure Matters: A Synchrotron Study Reveals How Crystallite Structure Influences the Deposition Mechanism for the Powder Aerosol Deposition Method, *J. Eur. Ceram. Soc.*, 2026, **46**, p 118127. https://doi.org/10.1016/j.jeurceramsoc.2026.118127
28. S. Lang, L. Hennerici, D. Kramer, D. Avadanii, S. Mück, M. Linz, J. Kita, R. Moos, and R. Mönig, Formation, Growth, and Shrinkage of Voids in Lithium Metal in Contact with an LLZO Electrolyte, *ACS Appl. Mater. Interfaces*, 2025, **17**, p 56980-56990. https://doi.org/10.1021/acsami.5c09594
29. J. Akedo, Aerosol Deposition Method for Fabrication of Nano Crystal Ceramic Layer, *MSF*, 2004, **449-452**, p 43-48. https://doi.org/10.4028/www.scientific.net/MSF.449-452.43
30. X. Liu, R. Garcia-Mendez, A.R. Lupini, Y. Cheng, Z.D. Hood, F. Han, A. Sharafi, J.C. Idrobo, N.J. Dudney, C. Wang, C. Ma, J. Sakamoto, and M. Chi, Local Electronic Structure Variation Resulting in Li 'filament' Formation within Solid Electrolytes, *Nat. Mater.*, 2021, **20**, p 1485-1490. https://doi.org/10.1038/s41563-021-01019-x
31. Y. Lu, X. Huang, Y. Ruan, Q. Wang, R. Kun, J. Yang, and Z. Wen, An in situ Element Permeation Constructed High Endurance Li-LLZO Interface at High Current Densities, *J. Mater. Chem. A*, 2018, **6**, p 18853-18858. https://doi.org/10.1039/c8ta07241h
32. X. Huang, Y. Lu, Z. Song, K. Rui, Q. Wang, T. Xiu, M.E. Badding, and Z. Wen, Manipulating Li_2O Atmosphere for Sintering Dense $Li_7La_3Zr_2O_{12}$ Solid Electrolyte, *Energy Storage Mater.*, 2019, **22**, p 207-217. https://doi.org/10.1016/j.ensm.2019.01.018
33. A. Sharafi, C.G. Haslam, R.D. Kerns, J. Wolfenstine, and J. Sakamoto, Controlling and Correlating the Effect of Grain Size with the Mechanical and Electrochemical Properties of $Li_7La_3Zr_2O_{12}$ solid-state Electrolyte, *J. Mater. Chem. A*, 2017, **5**, p 21491-21504. https://doi.org/10.1039/c7ta06790a
34. R.H. Basappa, T. Ito, and H. Yamada, Contact between garnet-type Solid Electrolyte and Lithium Metal Anode: Influence on Charge Transfer Resistance and short Circuit Prevention, *J. Electrochem. Soc.*, 2017, **164**, p A666-A671. https://doi.org/10.1149/2.0841704jes
35. F.M. Pesci, R.H. Brugge, A.K.O. Hekselman, A. Cavallaro, R.J. Chater, and A. Aguadero, Elucidating the Role of Dopants in the Critical Current Density for Dendrite Formation in Garnet Electrolytes, *J. Mater. Chem. A*, 2018, **6**, p 19817-19827. https://doi.org/10.1039/c8ta08366e
36. Y. Lu, C.-Z. Zhao, H. Yuan, X.-B. Cheng, J.-Q. Huang, and Q. Zhang, Critical Current Density in Solid-State Lithium Metal Batteries: Mechanism, Influences, and Strategies, *Adv. Funct. Mater.*, 2021, **31**, p 2009925. https://doi.org/10.1002/adfm.202009925
37. J.-F. Wu, W.K. Pang, V.K. Peterson, L. Wei, and X. Guo, garnet-type Fast Li-Ion Conductors with High Ionic Conductivities for All-solid-state Batteries, *ACS Appl. Mater. Interfaces*, 2017, **9**, p 12461-12468. https://doi.org/10.1021/acsami.7b00614
38. E. Rangasamy, J. Wolfenstine, and J. Sakamoto, The Role of Al and Li Concentration on the Formation of Cubic Garnet Solid Electrolyte of Nominal Composition $Li_7La_3Zr_2O_{12}$, *Solid State Ion.*, 2012, **206**, p 28. https://doi.org/10.1016/j.ssi.2011.10.022
39. J. Akedo, Room Temperature Impact Consolidation (RTIC) of Fine Ceramic Powder by Aerosol Deposition Method and Applications to Microdevices, *J. Therm. Spray Tech.*, 2008, **17**, p 181-198. https://doi.org/10.1007/s11666-008-9163-7
40. D. Paulus, J. Kita, and R. Moos, Relaxation Behavior of Intrinsic Compressive Stress in Powder Aerosol Co-deposited Films:

Rethinking PAD Films as Nanomaterials, *Ceram. Int.*, 2023, **49**, p 38375-38381. https://doi.org/10.1016/j.ceramint.2023.09.065
41. O. Sharifi, M. Golmohammad, M. Soozandeh, and A.S. Mehranjani, Improved Ga-Doped $Li_7La_3Zr_2O_{12}$ garnet-type Solid Electrolytes for solid-state Li-ion Batteries, *J. Solid State Electrochem.*, 2023, **27**, p 2433-2444. https://doi.org/10.1007/s10008-023-05522-w
42. D. Rettenwander, G. Redhammer, F. Preishuber-Pflügl, L. Cheng, L. Miara, R. Wagner, A. Welzl, E. Suard, M.M. Doeff, M. Wilkening, J. Fleig, and G. Amthauer, Structural and Electrochemical Consequences of Al and Ga Cosubstitution in $Li_7La_3Zr_2O_{12}$ Solid Electrolytes, *Chem. Mater.*, 2016, **28**, p 2384-2392. https://doi.org/10.1021/acs.chemmater.6b00579
43. J.T.S. Irvine, D.C. Sinclair, and A.R. West, Electroceramics: Characterization by Impedance Spectroscopy, *Adv. Mater.*, 1990, **2**, p 132-138. https://doi.org/10.1002/adma.19900020304
44. D. Rettenwander, A. Welzl, L. Cheng, J. Fleig, M. Musso, E. Suard, M.M. Doeff, G.J. Redhammer, and G. Amthauer, Synthesis, Crystal Chemistry, and Electrochemical Properties of $Li_{(7-2x)}La_3Zr_{(2-x)}Mo_{(x)}O_{12}$ (x = 0.1-0.4): Stabilization of the Cubic Garnet Polymorph via Substitution of Zr^{4+} by Mo^{6+}, *Inorg. Chem.*, 2015, **54**, p 10440-10449. https://doi.org/10.1021/acs.inorgchem.5b01895
45. R. Hongahally Basappa, T. Ito, T. Morimura, R. Bekarevich, K. Mitsuishi, and H. Yamada, Grain Boundary Modification to Suppress Lithium Penetration through garnet-type Solid Electrolyte, *J. Power. Sources*, 2017, **363**, p 145-152. https://doi.org/10.1016/j.jpowsour.2017.07.088
46. T. Krauskopf, H. Hartmann, W.G. Zeier, and J. Janek, Toward a Fundamental Understanding of the Lithium Metal Anode in Solid-State Batteries-an Electrochemo-Mechanical Study on the Garnet-Type Solid Electrolyte $Li_{6.25}Al_{0.25}La_3Zr_2O_{12}$, *ACS Appl. Mater. Interfaces*, 2019, **11**, p 14463-14477. https://doi.org/10.1021/acsami.9b02537
47. T. Krauskopf, F.H. Richter, W.G. Zeier, and J. Janek, Physicochemical Concepts of the Lithium Metal Anode in solid-state Batteries, *Chem. Rev.*, 2020, **120**, p 7745-7794. https://doi.org/10.1021/acs.chemrev.0c00431
48. C. Zhu, T. Fuchs, S.A.L. Weber, F.H. Richter, G. Glasser, F. Weber, H.-J. Butt, J. Janek, and R. Berger, Understanding the Evolution of Lithium Dendrites at $Li_{6.25}Al_{0.25}La_3Zr_2O_{12}$ Grain Boundaries via Operando Microscopy Techniques, *Nat. Commun.*, 2023, **14**, p 1300. https://doi.org/10.1038/s41467-023-36792-7
49. M. Linz, F. Bühner, D. Paulus, L. Hennerici, Y. Guo, V. Mereacre, U. Mansfeld, M. Seipenbusch, J. Kita, and R. Moos, Revealing the Deposition Mechanism of the Powder Aerosol Deposition Method Using Ceramic Oxide Core-Shell Particles, *Adv. Mater.*, 2024, **36**, p 2308294. https://doi.org/10.1002/adma.202308294
50. C.D. Fincher, C.E. Athanasiou, C. Gilgenbach, M. Wang, B.W. Sheldon, W.C. Carter, and Y.-M. Chiang, Controlling Dendrite Propagation in solid-state Batteries with Engineered Stress, *Joule*, 2022, **6**, p 2794-2809. https://doi.org/10.1016/j.joule.2022.10.011
51. N.H. Khansur, U. Eckstein, K. Riess, A. Martin, J. Drnec, U. Deisinger, and K.G. Webber, Synchrotron X-ray Microdiffraction Study of Residual Stresses in $BaTiO_3$ Films Deposited at Room Temperature by Aerosol Deposition, *Scripta Mater.*, 2018, **157**, p 86-89. https://doi.org/10.1016/j.scriptamat.2018.07.045
52. J. Adamczyk and P. Fuierer, Compressive Stress in Nano-crystalline Titanium Dioxide films by Aerosol Deposition, *Surf. Coat. Tech.*, 2018, **350**, p 542-549. https://doi.org/10.1016/j.surfcoat.2018.07.015
53. M. Schubert, J. Exner, and R. Moos, Influence of Carrier Gas Composition on the Stress of Al_2O_3 Coatings Prepared by the Aerosol Deposition Method, *Materials*, 2014, **7**, p 5633-5642. https://doi.org/10.3390/ma7085633
54. J. Neises, W.S. Scheld, A.-R. Seok, S. Lobe, M. Finsterbusch, S. Uhlenbruck, R. Schmechel, and N. Benson, Study of Thermal Material Properties for Ta- and Al-Substituted $Li_7La_3Zr_2O_{12}$ (LLZO) solid-state Electrolyte in Dependency of Temperature and Grain Size, *J. Mater. Chem. A*, 2022, **10**, p 12177-12186. https://doi.org/10.1039/d2ta00323f
55. M. Huang, T. Liu, Y. Deng, H. Geng, Y. Shen, Y. Lin, and C.-W. Nan, Effect of Sintering Temperature on Structure and Ionic Conductivity of $Li_{7-x}La_3Zr_2O_{12-0.5x}$ (x=0.5 ~ 0.7) Ceramics, *Solid State Ionics*, 2011, **204-205**, p 41-45. https://doi.org/10.1016/j.ssi.2011.10.003
56. J.S. Park, L. Cheng, V. Zorba, A. Mehta, J. Cabana, G. Chen, M.M. Doeff, T.J. Richardson, J.H. Park, J.-W. Son, and W.-S. Hong, Effects of Crystallinity and Impurities on the Electrical Conductivity of Li-La-Zr-O Thin Films, *Thin Solid Films*, 2015, **576**, p 55-60. https://doi.org/10.1016/j.tsf.2014.11.019
57. J. Exner, P. Fuierer, and R. Moos, Aerosol Deposition of (Cu,Ti) Substituted Bismuth Vanadate Films, *Thin Solid Films*, 2014, **573**, p 185-190. https://doi.org/10.1016/j.tsf.2014.11.037
58. F. Zhuo, U.R. Eckstein, N.H. Khansur, C. Dietz, D. Urushihara, T. Asaka, K. Kakimoto, K.G. Webber, X. Fang, and J. Rödel, Temperature-Induced Changes of the Electrical and Mechanical Properties of Aerosol-Deposited $BaTiO_3$ Thick Films for Energy Storage Applications, *J. Am. Ceram. Soc.*, 2022, **105**, p 4108-4121. https://doi.org/10.1111/jace.18377